Effect of Density Irregularities on Radio Frequency Wave Propagation in Ionospheric Plasmas

Eun-Hwa Kim [1,2*], *Jay R.* Johnson[2], *Syun'ichi* Shiraiwa[1], *Nicola* Bertelli[1], *Masayuki* Ono[1], and *Simon* Wing[3]

[1] Princeton Plasma Physics Laboratory, Princeton, New Jersey, USA
[2] Andrews University, Berrien Springs, Michigan, USA
[3] Applied Physics Laboratory, Johnson Hopkins University, Laurel, Maryland, USA

Abstract. Density irregularities play a vital role in determining how radio frequency (RF) waves travel through plasmas. In the Earth's ionosphere, these density irregularities also impact radio communication. In this study, we conduct a detailed numerical analysis of RF wave propagation in small-scale ionospheric density irregularities using the advanced Petra-M code. We focus specifically on high-frequency (HF) waves, ranging from 3 to 30 MHz, which are essential for military, amateur radio operators, and emergency communications. By introducing density structures, such as equatorial plasma bubbles derived from fluid simulations, we demonstrate that HF waves can scatter in multiple directions when they encounter these irregularities. Additionally, we observe significant mode conversion, where incoming electromagnetic waves transform into electrostatic modes within the density gradient layer. This shows that smaller density irregularities can greatly weaken signals or cause complete signal loss for receivers, emphasizing the need for increased awareness and innovative solutions in radio communication transmission.

1 Introduction

Radio frequency (RF) waves are significantly influenced by density irregularities such as filaments, instabilities, and turbulence within fusion devices. Similarly, in nature, plasma does not always change smoothly but exhibits turbulent structures. One example is the irregularities in ionospheric density.

The ionosphere extends from 100 to 2000 km above the thermosphere. Figure 1 illustrates an example of the ionospheric density profile from the International Reference Ionosphere. The ionosphere is divided into the E and F layers. The E-region, between 90 and 150 km altitude, primarily reflects lower-frequency radio waves. The F-region, located above 150 km, is a key layer for long-distance radio communication as it reflects higher-frequency radio waves [1].

One of the well-known ionospheric density irregularities at low latitudes is the equatorial plasma bubbles (EPBs). These EPBs are regions of reduced plasma density that form in the nighttime equatorial and low-latitude ionosphere. After sunset, rapid recombination at the bottomside F layer creates a steep density gradient, allowing Rayleigh–Taylor instability to develop and drive low-density structures upward through the denser plasma [2]. The spatial scale of fully developed EPB structures ranges from tens of kilometers to tens of centimeters [3, 4], which can be comparable to the typical wavelength of high-frequency (HF: 3 - 30 MHz) waves in the ionosphere.

HF radio waves are essential for long-distance communications. They are widely used for short-wave international broadcasting and by military and amateur radio operators. HF waves are also crucial for emergency communications [5]. Communication between ground stations using HF radio waves occurs through wave reflection and refraction in the ionosphere. Because solar and geomagnetic activities significantly influence the ionosphere, HF radio communications are affected by space weather [5].

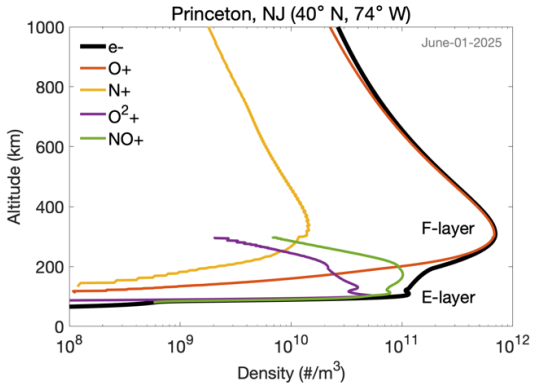

Fig. 1. Ionospheric plasma density at Princeton, NJ, USA, on 6/1/2025 obtained using the International Ionosphere Reference (https://kauai.ccmc.gsfc.nasa.gov/instantrun/iri).

* Corresponding author: ehkim@pppl.gov

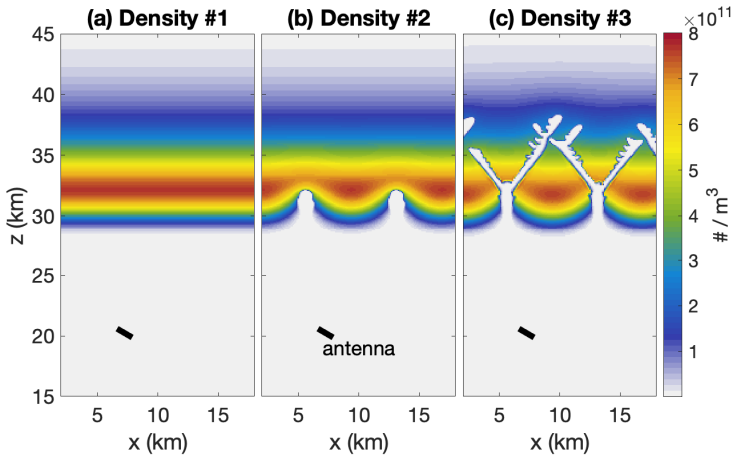

Fig. 2. (a) Assumed density structure without irregularity and (b)-(c) time evolution of EPB using numerical simulation [14,15] at t=1249.5s and t=1583.14s, respectively. We rescale the spatial domain to be 20 times smaller than the original dimension to consider smaller-scale density irregularities. Black bars represent the assumed location of the antenna.

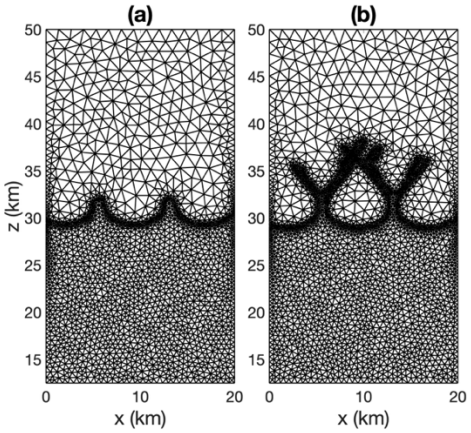

Fig. 3. Example of triangular meshes before refinement for density structures #2 and #3 in Figure 2 (b)-(c).

Currently, the effects of EPBs, such as power loss ratio, phase difference, and time delay, on HF radio communications are not well-documented through experimental data. To investigate these issues, several numerical simulations have been recently conducted [6-9].

Since the wavelength of the high-frequency (HF) wave in the ionosphere is significantly shorter than the overall ray path, many researchers employ the ray-tracing method [6, 7] for modeling purposes. However, this approach becomes ineffective when the irregularity size in the plasma is comparable to the wavelength, as it cannot precisely capture the complex interactions and deviations of ray paths through fluctuating density profiles. In such cases, a more sophisticated wave solution is required to accurately account for these effects.

Finite-difference time-domain (FDTD) wave simulation codes are capable of modeling ionospheric fluctuations and small-scale irregularities [8, 9], but they require very fine grid resolutions, which significantly increase computational cost and complexity. Alternatively, full-wave simulation codes based on the finite element method (FEM) can effectively overcome the limitations inherent in ray-tracing and FDTD approaches. FEM-based methods provide efficient and highly accurate solutions for wave propagation in highly inhomogeneous and dynamic plasma environments, making them particularly suitable for complex ionospheric modeling.

In this study, we investigate HF wave propagation within small-scale ionospheric density irregularities. To accomplish this, we perform comprehensive full-wave simulations utilizing the Petra-M code. Our research aims to provide deeper insights into how these irregularities influence wave behavior, which is crucial for improving communication and navigation systems that depend on ionospheric transmission.

2 Full-wave Simulations

The Petra-M is an open-source finite element method platform based on the scalable MFEM element library [10, 11]. It has been widely used for plasma wave simulations in fusion devices [12] and in Earth's magnetosphere [13]. Its accuracy has been well-verified through several code benchmarking activities [14]. In this study, we solve the cold plasma wave equation, including collision effects.

To describe the wave properties in the ionosphere, especially the small-scale density structures, we use the density instability profiles shown in Figure 2. We start with a smooth density profile that lacks irregularities, as seen in Figure 2(a). Next, we incorporate EPB profiles derived from simulations [15, 16]. Figures 2(b) and 2(c) show the time evolution of the EPBs at two different time steps. Since the original density profile resolution of 2 km is too coarse to capture small-scale density irregularities, we rescale the spatial domain to be 20 times smaller than the original. Such rescaling is reasonable because Rayleigh–Taylor–driven bubble dynamics are approximately self-similar in their nonlinear stage [17], and it is the relative scale of density structures to the Fresnel radius that controls wave propagation effects.

To consider the equatorial region, we assumed that the background magnetic field ($\mathbf{B}_0$) is aligned with the x direction and the ambient magnetic field strength $B_0 = 3.0 \times 10^{-5}$ T. Although the HF is defined as 3-30 MHz,

lower frequencies are often categorized as HF waves because their properties are similar. Thus, we launch 2MHz waves as in previous FDTD simulations [8]. These waves are launched obliquely from the antenna marked by black lines in Figure 2, with an elevation angle of 60° from the horizontal plane. We adopt a reflecting boundary condition with arbitrary collisional absorption near the left, right, and bottom boundaries. We also implemented constant collisions (with ν/ω = 0.005, where ν is the collisional frequency) between z = 25 km and 40 km. This approach helps prevent numerical singularities near the resonance and broadens the resonance.

We use fine meshes about 9.3 m- 10 m along the density gradient near z_{pe}, as shown in Figure 3, where the wave angular frequency (ω) matches the electron plasma frequency (ω_{pe}). For the given background conditions and frequency, ω_{pe} is much higher than the electron gyrofrequency (ω_{ce}); therefore, z_{pe} and z_{UH}, where $\omega = \omega_{UH}$ and ω_{UH} is the upper hybrid resonance frequency, are located close to each other. Above these density gradients at critical locations, HF waves become evanescent; therefore, we use larger meshes, with a maximum mesh size of approximately 75m. Below the density gradient, the 2MHz wavelength is approximately 150 m, and we use a mesh size that ranges from 10 to 20 m. The degrees of freedom are about 22 million for the simplest density case. The simulations are performed on a personal workstation with an Intel Xeon W5-2565X CPU at 3.2 GHz, with 12 processing cores and 512 GB of RAM. After generating the mesh, each FEM simulation takes roughly 800 seconds of CPU time.

Figure 4 shows the simulation results for density #1 shown in Figure 2(a). In this case, the electron density gradient aligns with the z direction; thus the electric field can be defined as parallel, $|E_{\parallel\nabla Ne}|=|E_z|$, and perpendicular, $|E_{\perp\nabla Ne}|=(|E_x|^2+|E_y|^2)^{1/2}$, to the density gradient (∇N_e). Figure 4 presents these electric field components of $|E_{\parallel\nabla Ne}|$ and $|E_{\perp\nabla Ne}|$. In this figure, the horizontal black lines indicate z_{pe}, and the vertical dotted lines mark x = 12.25 km, where the center of the ray reaches z_{pe}.

This figure shows that the wave launched at the antenna propagates toward the higher z direction and is reflected near z_{pe}. The amplitude of the reflected wave is significantly weaker than that of the incoming waves. We also find that wave power enhancement occurs near z_{pe}, especially in the parallel component to the density gradient ($|E_{\parallel\nabla Ne}|$). This power increase occurs in a thin layer, making it challenging to fully resolve the wave structure in this figure. To analyze these phenomena in detail, we plot the wave solution along the z direction in Figure 5(a). This figure clearly displays the power increase of $|E_{\parallel\nabla Ne}|$ in a narrow area between z_{pe} and z_{UH}. This power enhancement occurs due to the linear mode conversion from incoming electromagnetic (EM) waves into localized electrostatic (ES) modes [18].

Figure 5(b) illustrates the dispersion relation of waves at a frequency of 2 MHz with a normal angle of 60°. In this diagram, the red lines denote the right-handed polarized extraordinary (X) mode, while the left-handed polarized Z-mode is also represented, and the blue line corresponds to the left-handed polarized ordinary (O) mode. The lines labeled $z_{cut\text{-}R(L)}$ indicate the locations where the wave frequency ω matches the cutoff conditions, satisfying the equation $\omega^2 \mp \omega_{ce}\omega - \omega_{pe}^2 = 0$. When O- and X-waves propagate from the antenna and encounter the density gradient, they are reflected at the cutoff points z_{pe} or $z_{cut\text{-}R}$. However, since the gap between these cutoff points and the resonance layer is sufficiently narrow, mode conversion occurs from the O- and X-modes to the ES wave mode—characterized by an electric field component parallel to the density gradient—at a higher altitude between z_{pe} and z_{UH} [18, 19]. In this region, a substantial portion of the incoming wave energy is transferred to the resonance mode, resulting in a marked reduction in wave power reflected, as depicted in Figure 4. This process enhances energy coupling and influences wave propagation in the plasma.

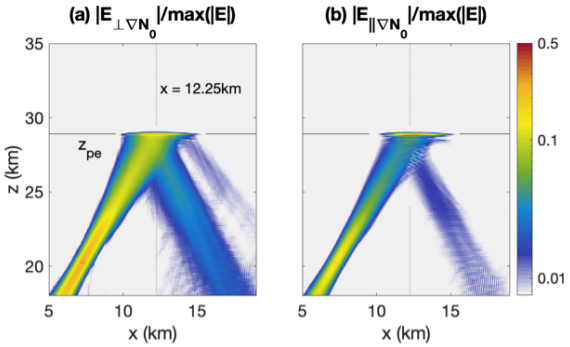

Fig. 4. Wave simulations for the density structure in Figure 2(a); Electric field power in (a) perpendicular ($|E_{\perp\nabla Ne}|$) and (b) parallel ($|E_{\parallel\nabla Ne}|$) to the density gradient (∇N_e). Here, the black horizontal lines represent z_{pe} where $\omega = \omega_{pe}$. At x=12.25 km (vertical dashed line), the ray reaches z_{pe}.

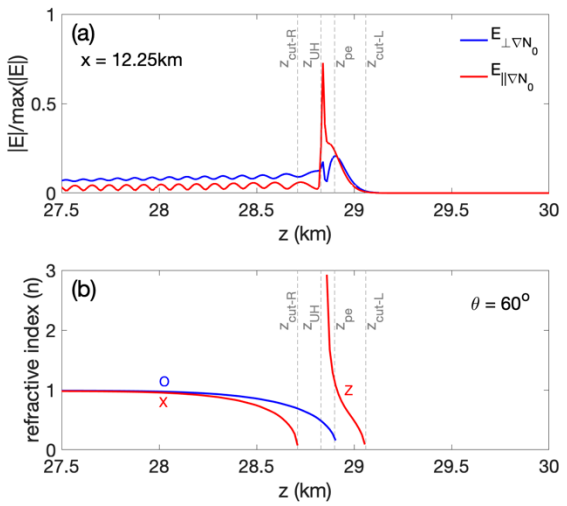

Fig. 5. (a) Wave solution along the z direction at x = 12.25km. Electrostatic waves occur in E⊥, which is parallel to the density gradient. (b) Wave dispersion relation of left-handed polarized ordinary (O, blue line), right-handed polarized extraordinary (X, red line), and left-handed polarized extraordinary (Z, red line) modes. Vertical lines represent that the incoming frequency matches the cutoff.

When density irregularities are introduced into the plasma, the resulting wave solutions become significantly more complex. Figure 6 illustrates wave propagation within density structure #2, as shown in

Figure 2(b). In this figure, panels (a) and (b) depict the total electric field strength, while panels (c) and (d) illustrate the electric field components in the x and z directions, respectively. When incoming waves encounter the plasma bubble, their ray paths become distorted due to the irregular density distribution. This distortion causes multiple reflections within the bubble, leading to complex wave interactions. Consequently, one reflected wave branch propagates nearly vertically from the top to the bottom of the density structure, and wave scattering also occurs, further complicating the waves within the plasma.

In Figure 6(b), we focus on the wave structure within the bubble, which is highlighted by a red box in panel (a). This detailed view allows us to observe the complex interactions of waves in that specific region. Additionally, the overplotted critical locations—z_{pe}, z_{UH}., $z_{cut\text{-}L}$, and $z_{cut\text{-}R}$—assist in identifying key points of interest along the vertical profile. A thin layer of wave power enhancement is visible between the heights z_{UH} and z_{pe}, indicative of energy buildup similar to the density structure observed in case #1.

Unlike Figure 4, Figures 6(c)-6(d) illustrate that both electric field powers of E_x and E_z are significantly enhanced near the resonance. This enhancement is primarily due to the noticeable density gradient present in both directions, which facilitates wave trapping and amplification. Additionally, the waves exhibit a broad range of wave normal angles, a consequence of multiple reflections within the medium. As a result, the reflected waves tend to have a much weaker amplitude compared to the incoming waves, since energy is distributed among multiple wave modes and pathways, leading to attenuation of the reflected component.

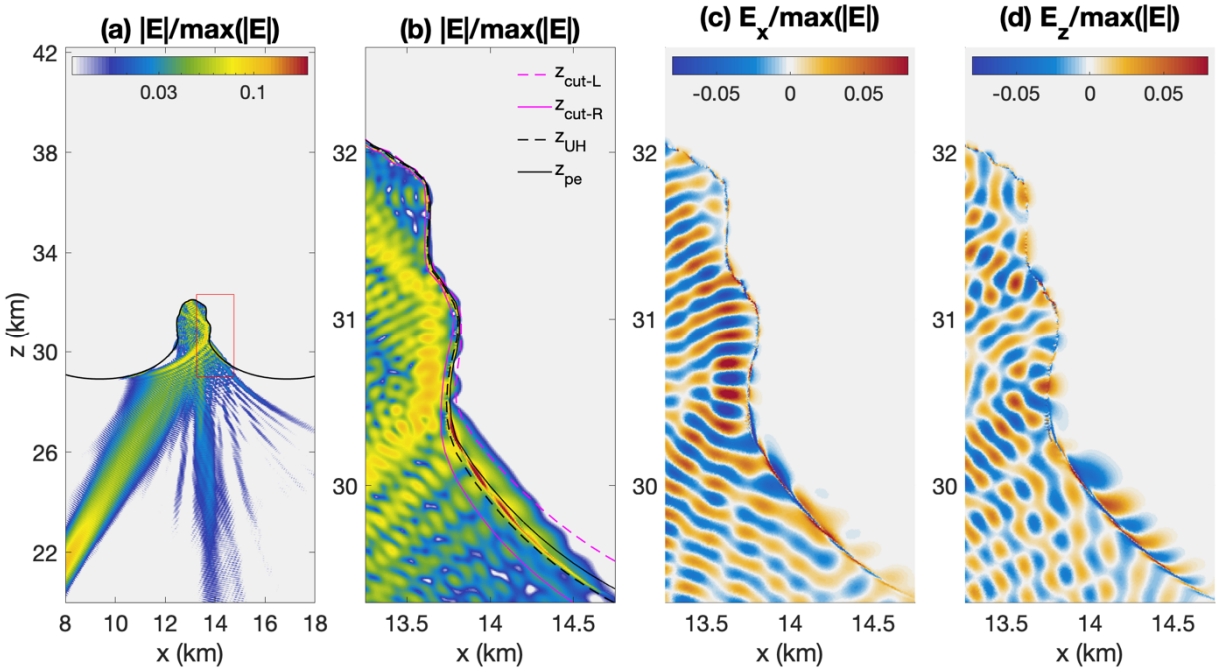

Fig. 6. Wave simulation results using the density structure #2 in Figure 2(b). (a)-(b) total electric field power (|E|), (c) E_x, and (d) E_z, respectively. In Panels (a) and (b), magenta dashed and solid lines are the cutoff conditions of Z and X modes, respectively, and black dashed and solid lines are the upper hybrid and electron plasma frequencies.

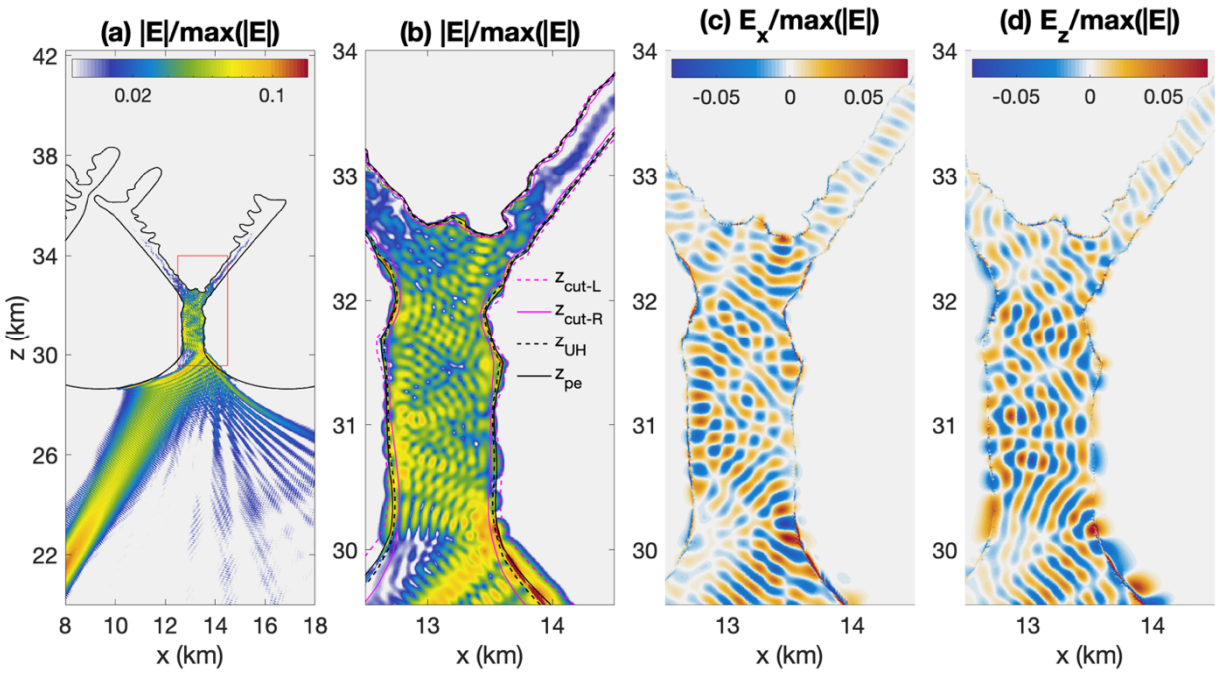

Fig. 7. Wave simulation results using the density structure #3 in Figure 2(c).

When adopting the most complex density structure depicted in Figure 7, the wave solution becomes considerably more intricate compared to the previous density cases. This figure illustrates clear signatures of wave reflection and refraction, as well as the presence of mode-converted electrostatic (ES) waves. These ES waves are visible in both components; however, when the density gradient predominantly orients along the x-axis—particularly near x = 13.6 km and z = 31 km—the ES mode experiences an amplification in the E_x component. This amplification occurs because E_x aligns nearly parallel to the density gradient at these specific locations. Furthermore, the waves can become trapped within the density structure, leading to sustained interactions. As shown in Figure 7(b), the wave power distribution indicates multiple horizontal reflections, and some wave packets penetrate the plasma bubble structure, reaching higher altitudes. Besides reflection, refraction, and mode conversion, wave trapping within the density structure and the subsequent propagation to higher altitudes contribute to potential power losses, affecting the overall transmission of wave energy.

The energy absorption near the density gradient and irregularities can be analyzed by comparing the Poynting flux. We examine the incoming and outgoing Poynting flux in the z direction (S_z) at z = 28 km, just below the density gradient area,

$$S^{\pm} = \int_{x=8\text{km}}^{x=18\text{km}} S_z^{\pm}(z = 28\text{km})dx.$$

Here, the ± signs represent Sz > 0 and Sz < 0, respectively. For the given conditions, the ratios of Density #1, #2, and #3 in Figure 2 are 8.1%, 6.7%, and 5.6%, respectively. This indicates that over 90% of energy can be absorbed and/or trapped within the density gradient. In the case of Density #1, most of the absorption occurs due to mode conversion, while the next two cases may be attributed to a combination of several factors described earlier.

It is noted that since we employed arbitrary density structures by simplifying the spatial scale from the plasma bubble simulation, these findings cannot be directly correlated with realistic HF wave propagation in the ionosphere. Furthermore, while we have effectively illustrated how wave energy is lost within the density irregularities, it remains challenging to clearly identify the specific contributions of trapping, refraction, and mode conversion to the overall wave absorption ratio. The efficiency of mode conversion is influenced by various factors, including density, spatial scale, angle of incidence with respect to the density gradient, and the background magnetic field [20, 21].

3 Summary

To better understand wave propagation within the small-scale structures of EPBs, we use the advanced full-wave simulation code Petra-M. Our research successfully demonstrates HF wave propagation with unstructured and non-uniform meshes, which are especially effective for modeling complex ionospheric phenomena. By leveraging the strengths of the finite element method, we efficiently generate detailed wave solutions that account for the varying ionospheric density. By incorporating density irregularities from equatorial plasma bubble simulations, we initiate HF wave sources and analyze their behavior.

Our findings reveal that small-scale plasma density irregularities play a crucial role in significantly altering the wave's propagation direction within the ionosphere. Specifically, these irregularities allow waves to penetrate the plasma bubble structures and reach higher altitudes, potentially causing multi-path delays in signal transmission leading to scintillations. Furthermore, waves can become trapped within the bubble, concentrating energy near the density gradients. In these regions, mode conversion occurs at the electron plasma

frequency, especially leading to significant conversion into electrostatic waves under the specific conditions studied. This mode conversion, alongside wave trapping, results in a reduction of radio power and is further influenced by ionospheric collisional absorption.

It is essential to note that our current simulations employ idealized parameters for the plasma bubbles, which may not accurately capture the complexity of natural conditions. To improve the realism of our models, future work should incorporate more accurate density structures derived from high-resolution simulations, such as those obtained with the SAMI3 model [22]. Integrating these detailed density profiles will enhance the predictive capability of our simulations and provide deeper insights into wave propagation dynamics in realistic ionospheric conditions.

Acknowledgement

The authors acknowledge support from the Department of Energy Contract No. DE-AC02-09CH11466, the National Science Foundation Grant No. AGS 2431664, and the NASA Grant No. 80NSSC21K1321.

References

1. K. G. Budden, The propagation of Radio Waves, Cambridge University Press (1985). https://doi.org/10.1017/CBO9780511564321
2. H. Kil, J. Astron, The Morphology of Equatorial Plasma Bubbles - a review, Space Sci. **32**, 13 (2015). http://doi.org/10.5140/JASS.2015.32.1.13
3. T. Yokoyama and C. Stolle, Low and Midlatitude Ionospheric Plasma Density Irregularities and Their Effects on Geomagnetic Field, Space Sci. Rev. **206**, 495–519 (2017). http://doi.org/10.1007/s11214-016-0295-7
4. S.-Y. Su, H. C. Yeh, and R. A. Heelis, ROCSAT 1 ionospheric plasma and electrodynamics instrument observations of equatorial spread F: An early transitional scale result, J. Geophys. Res. Space Physics **106**, 29153 (2001). http://doi.org/10.1029/2001JA900109
5. N. A. Frissell, J. S. Vega, E. Markowitz, A. J. Gerrard, W. D. Engelke, P. J. Erickson, E. S. Miller, R. C. Luetzelschwab and J. Bortnik, High-Frequency Communications Response to Solar Activity in September 2017 as Observed by Amateur Radio Networks, Space Weather **17**, 118–132, (2019). http://doi.org/10.1029/2018SW002008
6. M. A. Cervera, and T. J. Harris, Modeling ionospheric disturbance features in quasi-vertically incident ionograms using 3-D magnetoionic ray tracing and atmospheric gravity waves, J. Geophys. Res. Space Physics **119**, 431 (2014). http://doi.org/10.1002/2013JA019247
7. X. Ma, P. Guo and M. Wu, Simulation Research on the Influence of Plasma Bubbles on Radio Wave Propagation, Radio Science **58**, e2022RS007577 (2023). https://doi.org/10.1029/2022RS007577
8. D. R. Smith, T. Tan, E. Dao, C. Huang and J. J. Simpson, An FDTD Investigation of Orthogonality and the Backscattering of HF Waves in the Presence of Ionospheric Irregularities, J. Geophys. Res. Space Physics **125**, e2020JA028201 (2020). https://doi.org/10.1029/2020JA028201
9. A. Green, W. J. Longley, M. M. Oppenheim, M. A. Young, An open source code for modeling radio wave propagation in earth's ionosphere, Front. Astron. Space Sci. **12**, 1521497, (2025). https://doi.org/10.3389/fspas.2025.1521497
10. S. Shiraiwa, T. Fredian, J. Hillairet and J. Stillerman, πScope: Python based scientific workbench with MDSplus data visualization tool, Fusion Eng. Des. **112**, 835 (2016). http://doi.org/10.1016/j.fusengdes.2016.06.050
11. S. Shiraiwa, J. C. Wright, P. T. Bonoli, T. Kolev and M. Stowell, RF wave simulation for cold edge plasmas using the MFEM library, EPJ Web of Conferences **157**, 03048 (2017). http://doi.org/10.1051/epjconf/201715703048
12. N. Bertelli, S. Shiraiwa and M. Ono, 3D full wave fast wave modeling with realistic HHFW antenna geometry and SOL plasma in NSTX-U, Nucl. Fusion **62** 126046 (2022). http://doi.org/10.1088/1741-4326/ac9690
13. E.-H. Kim, S. Shiraiwa, J. R. Johnson, N. Bertelli, S. K. Vines, K.-H. Kim, M. Engebretson, H. Kim, and C. O'ffill, Propagation of EMIC Waves From Shabansky Orbits in the Dayside Magnetosphere, Geophys. Res. Lett. **52**, e2024GL113368 (2025). http://doi.org/10.1029/2024GL113368
14. N. Bertelli, S. Shiraiwa, W. Helou, D. Milanesio, W. Tierens, Benchmark between antenna code TOPICA, RAPLICASOL and Petra-M for the ICRH ITER antenna, AIP Conf. Proc. **2984**, 060006 (2023) https://doi.org/10.1063/5.0162415
15. C. Jiang, Chuajiang/Model-of-multi-ion-plasma-bubbles: V2.0. (V2.0) [Dataset], Zenodo (2023). https://doi.org/10.5281/zenodo.8008285
16. C. Jiang, L. Wei, T. Yokoyama, R. Tian, T. Liu, and G. Yang, J. Geophys. Modeling of Multi-Ion Plasma Bubbles in the Equatorial Ionosphere, J. Geophys. Res. Space Physics **128**, e2023JA031753 (2023). https://doi.org/10.1029/2023JA031753
17. Y. Zhou, Rayleigh–Taylor and Richtmyer–Meshkov instability induced flow, turbulence, and mixing. I, Physics Reports **720**, 1, (2017). https://doi.org/10.1016/j.physrep.2017.07.005

18. K.-S. Kim, E.-H. Kim, D.-H. Lee and K. Kim, plasmas, Conversion of ordinary and extraordinary waves into upper hybrid waves in inhomogeneous plasmas, Phys. Plasmas **12**, 052903 (2005). https://doi.org/10.1063/1.1896285
19. N. A. Gondarenko, P. N. Guzdar, S. L. Ossakow and P. A. Bernhardt, Linear mode conversion in inhomogeneous magnetized plasmas during ionospheric modification by HF radio waves, J. Geophys. Res. Space Physics **108**, 1470 (2003). http://doi.org/10.1029/2003JA009985
20. E.-H. Kim, I. H. Cairns and P. A. Robinson, Extraordinary-Mode Radiation Produced by Linear-Mode Conversion of Langmuir Waves, Phys. Rev. Lett. **99**, 015003 (2007). http://doi.org/10.1103/PhysRevLett.99.015003.
21. E.-H. Kim, I. H. Cairns, and J. R. Johnson, Linear mode conversion of Langmuir/z-mode waves to radiation in plasmas with various magnetic field strength, Phys. Plasmas **20**, 122103 (2013). https://doi.org/10.1063/1.4837515
22. J. D. Huba, G. Joyce, and J. Krall, Three-dimensional equatorial spread F modelling, Geophys. Res. Lett. **35**, L10102 (2008). http://doi.org/10.1029/2008GL033509